processes

MDPI

Article

Interfacial Adsorption Mechanism of Diethyldithiocarbamate in High-Sulfur Residue Flotation

Hong Liu [1], Jing He [1], Tao Luo [1], Jie Dai [1], Shuqiong Cao [1], Shenghai Yang [1,2], Chaobo Tang [1], Changhong Wang [1,*] and Yongming Chen [1,2,*]

[1] School of Metallurgy and Environment, Central South University, Changsha 410083, China; lh943983603@csu.edu.cn (H.L.); he6213@csu.edu.cn (J.H.); 15273376510@163.com (T.L.); 213501018@csu.edu.cn (J.D.); m15274795915@163.com (S.C.); yangshcsu@163.com (S.Y.); chaobotang@163.com (C.T.)

[2] Hunan Provincial Key Laboratory of Nonferrous Value-Added Metallurgy, Changsha 410083, China

* Correspondence: changhong.wang@csu.edu.cn (C.W.); csuchenyongming@163.com (Y.C.)

Abstract: Diethyldithiocarbamate (DDTC) is employed in the sulfide ore flotation process due to its excellent collection performance. Herein, we investigated the interfacial adsorption behavior of DDTC on the four main mineral phases of high-sulfur residue: sulfur, pyrite, sphalerite, and lead sulfate. The adsorption behavior of DDTC and H_2O, namely, the adsorption structure and the energy and electron localization function cross section, were explored using density function theory calculation. The results were helpful in constructing a coadsorption model of DDTC and H_2O, which was validated by pure mineral flotation and characterization of Fourier transform infrared spectra. The coadsorption model indicated that the adsorption of DDTC on sulfur, sphalerite, and lead sulfate was weak with physical bonding, while its adsorption on pyrite was strong with chemical bonding. Practical bench-scale high-sulfur residue flotation was performed, and the result was different from that obtained from pure mineral flotation. Our developed model predictions and mineral fugacity pattern analysis were synergistically used to explain this difference. Overall, this work proposes for the first time a coadsorption model of DDTC and H_2O and provides important insights into interfacial adsorption in high-sulfur residue flotation.

Keywords: flotation; high-sulfur residue; diethyldithiocarbamate; DFT; coadsorption model

check for updates

Citation: Liu, H.; He, J.; Luo, T.; Dai, J.; Cao, S.; Yang, S.; Tang, C.; Wang, C.; Chen, Y. Interfacial Adsorption Mechanism of Diethyldithiocarbamate in High-Sulfur Residue Flotation. *Processes* **2023**, *11*, 1568. https://doi.org/10.3390/pr11051568

Academic Editor: Haiping Zhu

Received: 6 April 2023
Revised: 16 May 2023
Accepted: 19 May 2023
Published: 21 May 2023

Copyright: © 2023 by the authors. Licensee MDPI, Basel, Switzerland. This article is an open access article distributed under the terms and conditions of the Creative Commons Attribution (CC BY) license (https://creativecommons.org/licenses/by/4.0/).

1. Introduction

Zinc hydrometallurgy is the main pathway for extracting zinc metal from zinc sulfide concentrate. It is divided into conventional and direct routes. The direct route includes the steps of oxygen pressure/atmospheric pressure leaching, purification, and electrodeposition, which adopts whole-wet technology and avoids the high-temperature process of oxidizing roasting. In the leaching process, the solid sulfur enters the residue phase, thus avoiding emission of polluted SO_2 gas. However, the sulfur content in the leaching residue [1] is generally as high as 40–60%. This has attracted extensive studies aimed at recycling it.

The flotation–hot filtration method [2,3] is predominantly used for recycling sulfur in the high-sulfur residue due to its simple process, low-cost production, and feasible scale-up. Therefore, it has been widely used in the oxygen pressure leaching of zinc refineries [4–7]. However, this approach causes low sulfur grade in the concentrate. For instance, Liu et al. [1] explored the trapping ability of xanthate, dithiophosphate, and isopropyl ethyl thiocarbamate on sulfur in the high-sulfur residue. The sulfur recovery rates by xanthate, dithiophosphate, and isopropyl ethyl thiocarbamate were as high as 93.67, 97.83, and 99.87%, respectively, while the resultant sulfur grades in the concentrate were as low as 81.53, 82.25, and 84.47%, respectively. An effective approach to address this challenge is to introduce suitable flotation agents [8,9] into the targeted solution. As a

flotation agent, the collector serves to improve collection efficiency of the target mineral phases and promote their separation. Generally, the collector is composed of mineral-friendly and hydrophobic groups, with the former supporting its adsorption on the mineral phase, thereby changing the hydrophilicity and floatability.

Diethyldithiocarbamate (DDTC) [10] is a robust collector used in sulfide ore flotation that has a strong collection ability [11]. Niu et al. [12] found that DDTC could significantly improve the separation efficiency of pyrite and galena in a high-alkaline lime system. Zhang et al. [13] found that adding DDTC caused desirable flotation performance in jamesonite despite the wide range of pH of 2–13. Fourier transform infrared spectra (FT-IR) characterization showed that DDTC adsorbed on the surface of jamesonite in the form of lead diethyldithiocarbamate. Cui et al. [14] used a mixed collector containing diisobutyl dithiophosphate and DDTC to improve the flotation performance of jamesonite, which resulted in an improved recovery of 98.85% of jamesonite. Another interesting finding was that the combination of DDTC and butyl xanthate significantly improved the stability of foam during the flotation process, which increased the volume of maximum foam layer by 102% and prolonged the half-life of the foam by 129% [15]. However, despite extensive studies on the technical feasibility and improvement of the flotation process with DDTC, there is a knowledge gap on its mechanism. The capture mechanism of DDTC on the targeted mineral is closely associated with its adsorption mechanism, which influences its trapping performance. Greater understanding of this process would help further improve the flotation process.

In recent times, density function theory (DFT) calculation has become an important method to study adsorption performance on the mineral phase at a molecular level. For instance, Liu et al. [1] studied the adsorption properties of xanthate, dithiophosphate, and isopropyl ethyl thiocarbamate on the mineral phase of high-sulfur residue. Zhang et al. [16] studied the flotation separation performance of dithiophosphate galena and sphalerite using DFT calculations. Chen et al. [17] investigated the thermodynamics of xanthate, dithiophosphate, and dithiocarbamate adsorption on galena and pyrite surfaces using the DFT method. Dai et al. [18] studied the adsorption of butyl xanthate on arsenopyrite (001) and Cu^{2+}-activated arsenopyrite (001) surfaces using the DFT method. Huang et al. [19] used theoretical chemical knowledge to modify xanthate collectors and used DFT calculations to predict the performance of modified xanthate collectors. Therefore, DFT calculations have become an important method to study the adsorption of collectors on mineral surfaces.

In this work, we investigated the interfacial adsorption of DDTC on the four main mineral phases present in high-sulfur residue: sulfur, pyrite, sphalerite, and lead sulfate. Firstly, the adsorption behavior of DDTC and H_2O, namely, the adsorption structure and energy and electron localization function (ELF) cross section, on the four minerals phases were explored using DFT calculation. Then, a coadsorption model of DDTC and H_2O was constructed using DFT calculation, which was validated by pure mineral flotation and FT-IR results. Finally, practical bench-scale high-sulfur residue flotation was performed, the result of which was elucidated synergistically using our developed model and mineral fugacity pattern analysis. Overall, this study proposes for the first time a validated coadsorption model of DDTC and H_2O and provides insights into the interfacial adsorption mechanism in high-sulfur residue flotation. More importantly, this work provides important reference on the recovery of targeted minerals in unconventional sulfide flotation processes.

2. Methods

2.1. DFT Calculation

A structure search on the DDTC molecule was performed in the open-source Xtb software developed by the Grimme group [20,21]. Then, its structure was further optimized in the Gaussian package. Specifically, the DDTC molecule was optimized in the base group of m062x/6-311++g(2d, p), where the number of functions with certain properties used to describe the wave function of the system reflected the accuracy of the calculation. It

was then subjected to frequency calculations to determine its structure plausibility. The surface electrostatic potentials of DDTC were calculated in Multiwfn software [22] (details in Supplemental Material S1).

The high-sulfur residue contained four main mineral phases: sulfur, sphalerite, pyrite, and lead sulfate. The most stable surface of sulfur $S_{(110)}$, sphalerite $ZnS_{(110)}$, pyrite $FeS_{2(100)}$, and lead sulfate $PbSO_{4(001)}$ were intercepted [1,23,24]. The surface was optimized in a restricted way, relaxing one surface and three layers of atoms in each mineral phase. The thickness of the vacuum layer during the relaxation process was 20 Å. The optimized structure is shown in Figure 1.

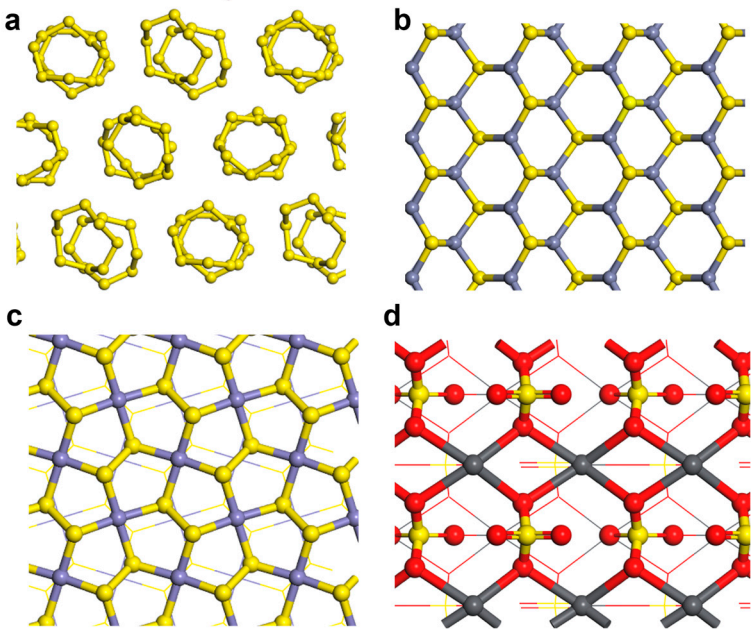

Figure 1. Optimized surface structure of the four mineral phases. (**a**) $S_{(110)}$; (**b**) $ZnS_{(110)}$; (**c**) $FeS_{2(100)}$; (**d**) $PbSO_{4(001)}$.

The adsorption process on the mineral phase surface was simulated and calculated in the DFT software VASP (Figure 2). Generalized gradient approximation, where the approximate method of exchanging correlation functions reflected the accuracy of the calculation, was used for the exchange correlation generalization. The pseudopotential was Perdew–Burke–Ernzerh (PBE), a virtual potential introduced in the numerical calculation of the energy band structure. The surface was optimized by the conjugate gradient method with a plane wave truncation energy of 400 eV. The Monkhorst–Pack method was used to generate a $3 \times 3 \times 1$ K-point grid. The energy convergence threshold for the self-consistent field iteration of the surface optimization was 10^{-5} eV. The geometry optimization criterion was less than 0.05 eV/Å per atom around the force (details in Table S1).

After optimization of the H_2O and DDTC adsorption models, self-consistent calculations were performed to obtain accurate electronic structure information. The electron localization function (ELF) [16,25] was subsequently obtained in VESTA software [26]. ELF is a common method to characterize bonds formed between atoms. The molecular orbitals generated by DFT calculation were denoted as canonical molecular orbitals (canonical MO). The MOs tended to be nonlocalized and therefore did not correspond to chemical bonds. To directly link the orbitals to the chemical bonds, we transformed MO into localized molecular orbital (localized MO (LMO)). ELF is a common method to localize orbitals. When the value of ELF is close to 1 between two atoms, this implies that there are localized electrons and thus a chemical bond between them.

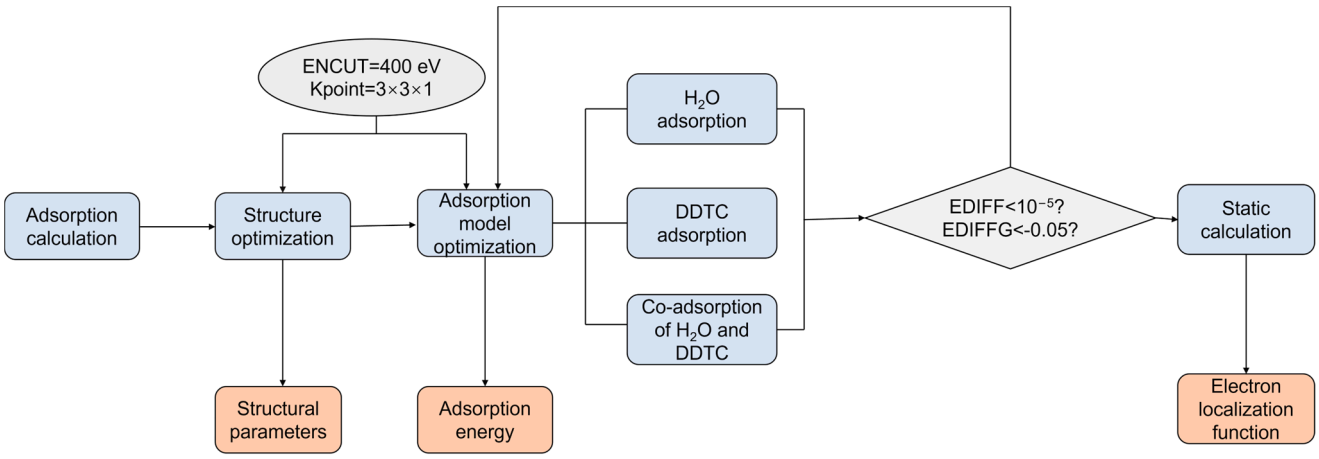

Figure 2. Adsorption calculation of DDTC/H_2O.

2.2. Material and Reagents

2.2.1. High-Sulfur Residue

The composition of the high-sulfur residue was analyzed by inductively coupled plasma emission spectrometer (ICP), and the results are recorded in Table 1. The phase of the high-sulfur residue was analyzed by X-ray diffraction (XRD), and the results are shown in Figure 3. The results indicated that the high-sulfur residue contained mainly contained S, Fe, Zn, Pb, Ca, and other elements. The main phases in the high-sulfur residue were sulfur (almost 32.98%), sphalerite, and pyrite.

Table 1. Elemental composition of the high-sulfur residue measured by ICP (wt.%).

Element	S *	Fe	Zn	Mg	Mn	Pb	Al	Ca	S #
Content	38.20	16.90	4.72	0.68	0.35	2.65	0.32	1.37	32.98

* Infrared carbon sulfur meter test results; # detection results of carbon tetrachloride ultrasound extraction.

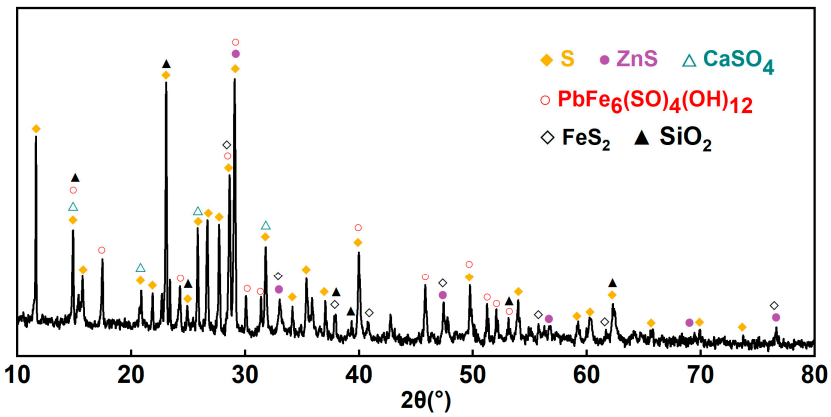

Figure 3. XRD of high-sulfur residue.

2.2.2. Pyrite

The composition of the pyrite sample was analyzed by ICP, and the results are recorded in Table 2. The phase of the pyrite was analyzed by XRD, and the results are shown in Figure 4. The ICP results indicated that the pyrite samples used in the experiment contained Fe and S. The sum of the two elements amounted to 98.72%. The XRD results indicated the pyrite samples to be pure.

Table 2. Elemental composition of the pyrite sample measured by ICP (wt.%).

Element	Fe	S *	Others
Content	46.23	52.49	1.28

* Barium sulfate gravimetric method test results.

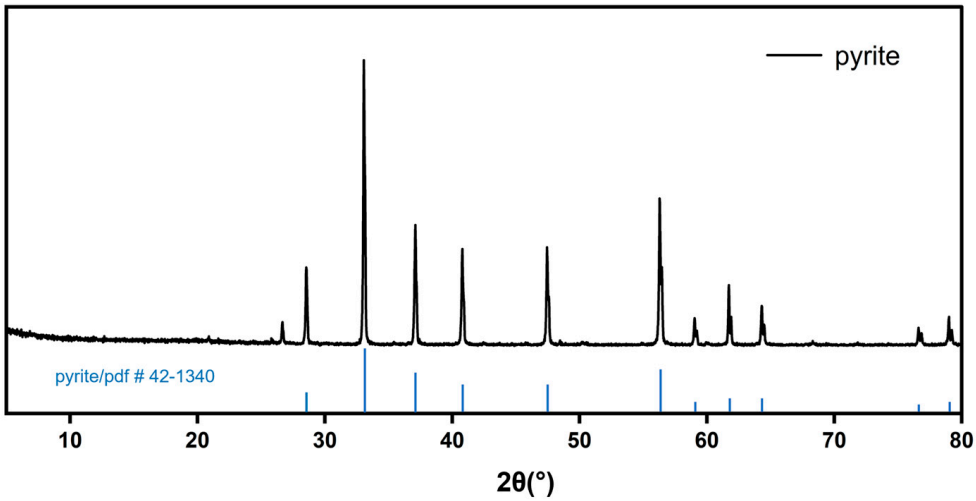

Figure 4. XRD of pyrite.

2.2.3. Reagents

Details of other reagents are shown in Table 3.

Table 3. Main reagent information.

Reagents	Molecular Formula	Standard	Manufacturer
DDTC	$C_4H_{12}NCSSNa$	AR	Tianjin Kemiou Chemical Reagent Co., Ltd., Tianjin, China
Sulfur	S	AR	Tianjin Kemiou Chemical Reagent Co., Ltd., Tianjin, China
Lead sulfate	$PbSO_4$	AR	Tianjin Kemiou Chemical Reagent Co., Ltd., Tianjin, China
Sphalerite	ZnS	AR	Tianjin Kemiou Chemical Reagent Co., Ltd., Tianjin, China
Terpineol	$C_{10}H_{11}OH$	Industrial	Tianjin Kemiou Chemical Reagent Co., Ltd., Tianjin, China

2.3. Mineral Flotation Evaluation

2.3.1. Pure Mineral Flotation

The flotation tests were carried out in a 1.5L XFD pure-cell flotation machine, and 150 g of raw materials were weighed each time to prepare a 10% solid–liquid suspension. The DDTC concentrations were 0, 100, 200, 300, 400, and 500 g/t. The flotation temperature was 25 °C, the air volume flow rate was 300 L/h, the slurry pH was 8, and the flotation time was 10 min. The corresponding flotation agents were added to the flotation machine according to the experimental requirements. For the pure mineral tests, the weighing method was used to calculate the flotation recovery rate.

2.3.2. Adsorption Behavior of DDTC on Pure Minerals

First, 10 g of minerals was taken in a beaker, and the pulp concentration was then adjusted to be 10% material liquid. DDTC was added in a beaker, with the concentration of

DDTC being 300 g/t and pH = 8. The slurry was stirred at 25 °C for 30 min and filtered. The filtered residue was washed three times and dried for subsequent characterization. Nicolet 6700 Fourier transform infrared spectroscopy (FT-IR, Thermo Fisher Scientific, Waltham, MA, USA) was used to analyze the surface structure before and after the interaction of DDTC with pure minerals.

2.3.3. High-Sulfur Residue Flotation

The test conditions were 15% solid–liquid suspension, flotation time 15 min, pulp temperature 25 °C, air volume flow rate 300 L/h, pH = 8, and DDTC concentrations 100, 200, 300, 400, or 500 g/t. After the flotation process, the sample was filtered. The residue was washed and dried for characterization.

2.3.4. Analysis and Characterization

The sulfur was extracted using the carbon tetrachloride method. First, 0.100–0.150 g of dry material was added to carbon tetrachloride for 20 min of sonication. Then, the filtered residue sample was put into a platinum tray and steam-dried for weight quantification. The sulfur content in the high-sulfur residue was determined using the carbon tetrachloride microwave method. To ensure test accuracy, a mean value obtained from three tests was collected as the final result.

The composition of the high-sulfur residue and pyrite was analyzed by inductively coupled plasma emission spectrometer (PerkinElmer Optima 8300, Waltham, MA, USA). X-ray fluorescence spectroscopy (PANalytical Axios, Almelo, The Netherlands) was used to perform semiquantitative analysis of various element distributions in the concentrate and tailings.

SEM–EDS (MIRA4 LMH from TESCAN, Brno, Czech Republic) was used to characterize the morphology in the concentrate and tailings after high-sulfur residue flotation.

3. Results and Discussion

3.1. Coadsorption Model of DDTC and H_2O

3.1.1. Adsorption Behavior of DDTC

First, we explored the adsorption structure and energy and ELF cross section of DDTC on the main minerals in the high-sulfur residue (Figure 5). When adsorption of DDTC appeared on sulfur, the distance between their respective inner sulfur atoms was between 3.47 and 4.75 Å with adsorption energy of −6.65 kJ/mol (Figure 5a). This meant a physical adsorption with a weak bond of DDTC onto the sulfur surface [27].

For DDTC adsorption on pyrite, the sulfur atoms S1 and S2 in the polar group of DDTC prompted a shift of the iron atoms Fe1 and Fe2 on pyrite from an original coordination unsaturated structure to a saturated six-coordination structure (Figure 5b). This decreased the surface energy on pyrite. The adsorption energy of DDTC on pyrite was calculated as −195.64 kJ/mol, which meant a strong adsorption on pyrite. As shown in Figure 5e, the ELF value between the sulfur atom and the iron atom was close to 1. This indicated the existence of localization electrons between them, which formed a chemisorption.

DDTC adsorption on sphalerite was similar to that on pyrite (Figure 5c). The adsorption energy of DDTC on sphalerite was calculated as −42.57 kJ/mol. Figure 5f also shows chemisorption characteristics of DDTC on sphalerite.

For DDTC adsorption on lead sulfate, S1 and S2 on DDTC were adsorbed on lead atoms with an adsorption energy of −81.05 kJ/mol (Figure 5d). This indicated a strong adsorption of DDTC on lead sulfate. Meanwhile, as shown in Figure 5g, DDTC was chemisorbed on the surface of lead sulfate.

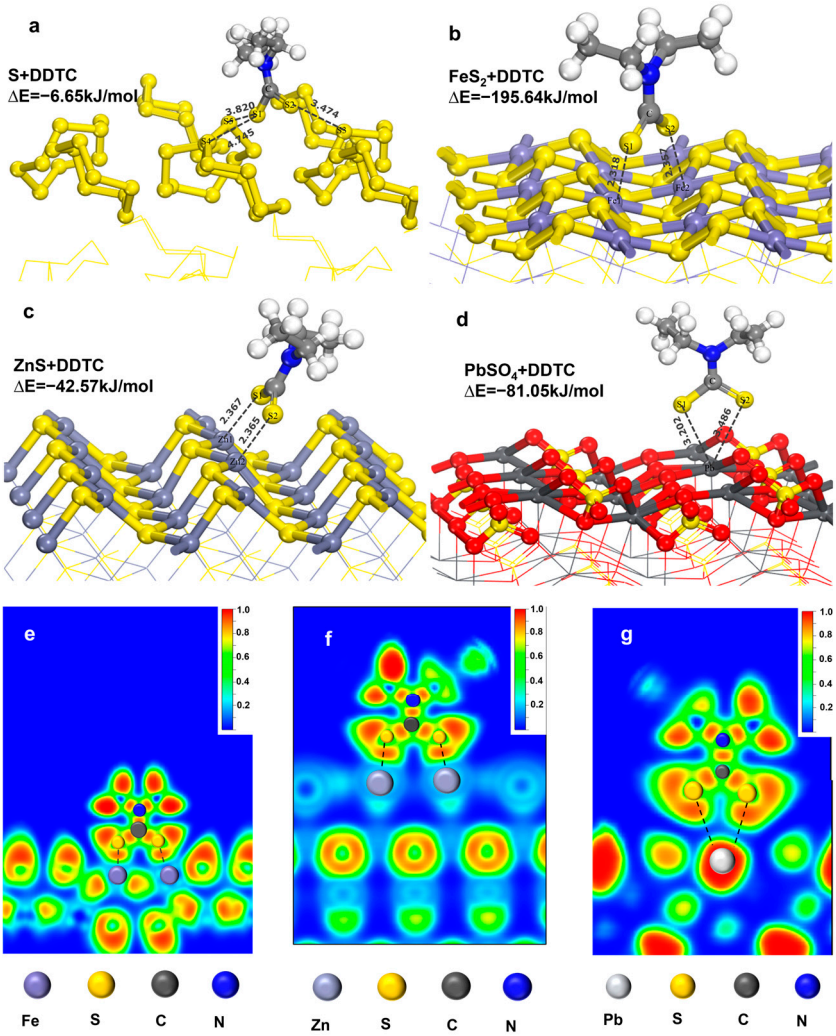

Figure 5. Adsorption structure and energy and ELF of DDTC on the main minerals in the high-sulfur residue. (**a**) Sulfur; (**b**) pyrite; (**c**) sphalerite; (**d**) lead sulfate; (**e**) ELF of pyrite; (**f**) ELF of sphalerite; (**g**) ELF of lead sulfate.

3.1.2. Adsorption Behavior of H_2O

Next, we investigated the adsorption structure and energy and ELF cross section of H_2O on the main mineral phase of the high-sulfur residue (Figure 6). For adsorption of H_2O on sulfur, the distances of the oxygen atom O and hydrogen atoms H1 and H2 with the sulfur atom S were relatively far (Figure 6a). This caused a physical adsorption with a low adsorption energy of −8.49 kJ/mol.

For H_2O adsorption on sphalerite, oxygen atoms adsorbed on zinc atoms, while hydrogen atoms adsorbed on sulfur atoms (Figure 6b). The adsorption energy was calculated as −65.05 kJ/mol, which was close to the −65.5 kJ/mol calculated by Sit et al. [28] using Quantum-ESPRESSO under PBE pseudopotential. As shown in Figure 6e, there was a high ELF value between oxygen atoms and zinc atoms, indicating chemisorption of H_2O on sphalerite. On the other hand, the ELF value between the hydrogen atoms and the sulfur atoms was nearly 0, which indicated electrostatic interaction.

For H_2O adsorption on pyrite, the oxygen atoms adsorbed on the iron atoms, while the hydrogen atoms adsorbed on the sulfur atoms (Figure 6c). The adsorption energy was calculated as −62.71 kJ/mol, which was close to the adsorption energy on sphalerite. This indicated a close adsorption ability of H_2O on sphalerite and pyrite. This adsorption energy was also close to the −62 kJ/mol obtained by Pollet et al. [29] using ab initio molecular dynamics simulations. There was a high ELF value between oxygen atoms and

iron atoms (Figure 6f), indicating that the adsorption of H_2O on the surface of pyrite was chemisorption. At the same time, the hydrogen atoms in H_2O and the sulfur atoms on pyrite had mutual electrostatic interaction.

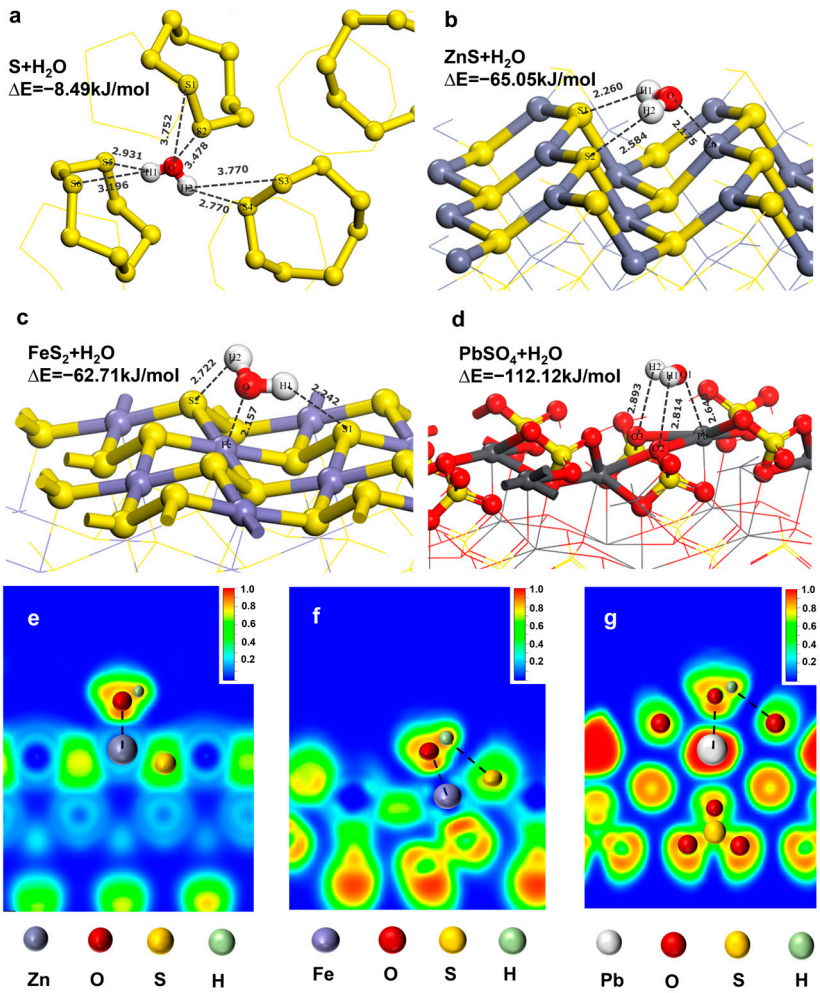

Figure 6. Adsorption of H_2O on the main mineral phase in the high-sulfur residue. (**a**) Sulfur; (**b**) sphalerite; (**c**) pyrite; (**d**) lead sulfate; (**e**) ELF of sphalerite; (**f**) ELF of pyrite; (**g**) ELF of lead sulfate.

For H_2O adsorption on lead sulfate, oxygen atoms adsorbed on lead atoms, while hydrogen atoms adsorbed on oxygen atoms (Figure 6d). The adsorption energy was as high as −112.12 kJ/mol, which suggested a strong adsorption. This was confirmed by the result showing H_2O was chemisorbed on the lead sulfate (Figure 6g).

3.1.3. Coadsorption Model of DDTC and H_2O

After understanding the adsorption behavior of DDTC and H_2O on sulfur, pyrite, sphalerite, and lead sulfate, we further constructed their coadsorption model to gain more insight into the interfacial adsorption mechanism. On sulfur, both H_2O and DDTC had weak adsorption ability, indicating that the sulfur was hydrophobic and could not be well trapped by DDTC. On sphalerite and lead sulfate surfaces, H_2O preferentially adsorbed on metal atoms than DDTC. However, on pyrite, DDTC preferentially adsorbed on metal ions than H_2O. Overall, the coadsorption models of DDTC and H_2O on sulfur, sphalerite, pyrite, and lead sulfate were established, which depended on their mutual adsorption ability gap.

H_2O had different degrees of influence on the adsorption of DDTC on different carriers (Figure 7). For instance, on sulfur, H_2O had little influence on the adsorption structure and energy of DDTC (decreasing from −6.65 to −6.13 kJ/mol). On sphalerite, the adsorption energy of DDTC was significantly weakened from −42.57 to −8.08 kJ/mol, and

its adsorption mode transformed from chemisorption to physical adsorption (Figure 7b). This was due to the adsorption of H_2O around the zinc atoms of sphalerite. On pyrite, the adsorption energy of DDTC changed slightly from −195.64 to −191.46 kJ/mol with consistent chemisorption (Figure 7c). This indicated the little impact of H_2O. On the surface of lead sulfate, H_2O was preferentially adsorbed. DDTC was adsorbed on the surface of lead sulfate by electrostatic interaction with H_2O, which is a kind of indirect adsorption (Figure 7d). The adsorption energy of DDTC significantly weakened from −81.05 to −18.53 kJ/mol.

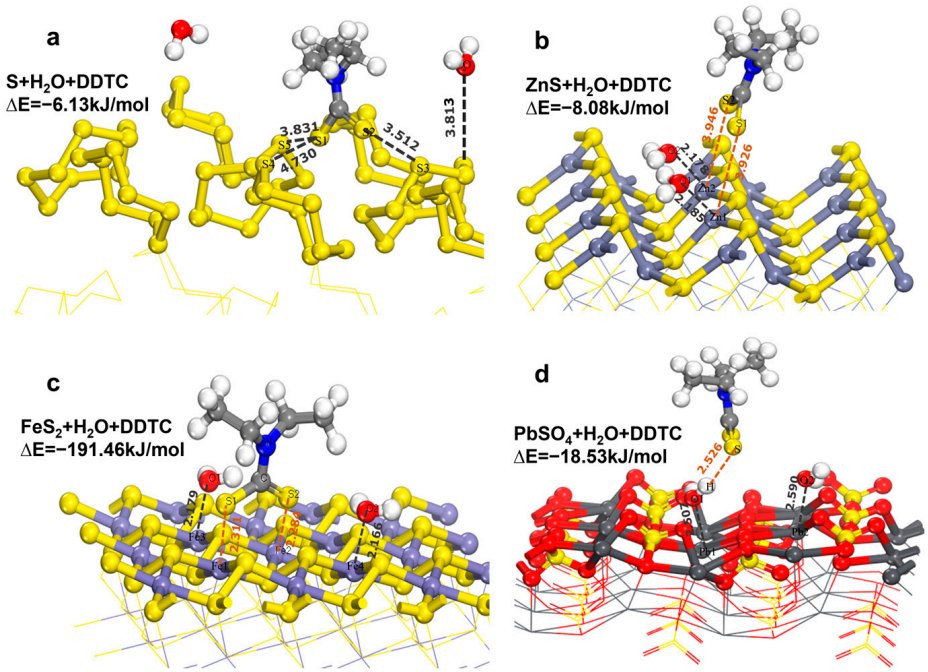

Figure 7. Coadsorption model between DDTC and H_2O on the mineral surface. (**a**) Sulfur; (**b**) sphalerite; (**c**) pyrite; (**d**) lead sulfate.

Based on the above, the DDTC adsorption on sulfur, sphalerite, and lead sulfate was weak with physical bonding, while its adsorption on pyrite was strong with chemical bonding.

3.2. Model Validation

Pure mineral flotation was performed to validate the coadsorption model (Figure 8). In the absence of DDTC, sulfur had almost 100% recovery, indicating excellent flotation performance, while sphalerite, pyrite, and lead sulfate had low recoveries, indicating that these minerals had good hydrophilic properties. With increasing DDTC concentration from 0 to 500 g/t, the recovery of sulfur, sphalerite, and lead sulfate saw little change, while the recovery of pyrite increased significantly. After the addition of DDTC, the recovery of pyrite increased by nearly 60% compared to that without DDTC. This indicated that DDTC had weak ability to trap sulfur, sphalerite, and lead sulfate but had the desired ability to trap pyrite. This result was consistent with the result of the coadsorption model: the interaction of DDTC on sulfur, sphalerite, and lead sulfate was weak adsorption, while the interaction of DDTC on pyrite was strong adsorption.

The FT-IR results of DDTC adsorbed on the main minerals further validated the coadsorption model (Figure 9). The peaks around 3000 cm^{-1} in DDTC were C–H vibrational peaks, and the peaks at 1262.0, 1414.6, and 1476.4 cm^{-1} were associated with C–N vibrations. The FT-IR spectra of DDTC were nearly unchanged before and after its adsorption on sulfur. This indicated almost no occurrence of DDTC adsorption on sulfur. The weak peaks in the FT-IR spectra of sphalerite and lead sulfate after DDTC treatment indicated that DDTC was physically adsorbed on them. The FT-IR spectra of pyrite showed absorption peaks of

C–N vibrations and a new peak at 1490.2 cm^{-1} after DDTC treatment, which indicated its chemisorption on pyrite. Overall, the FT-IR result agreed well with the coadsorption model.

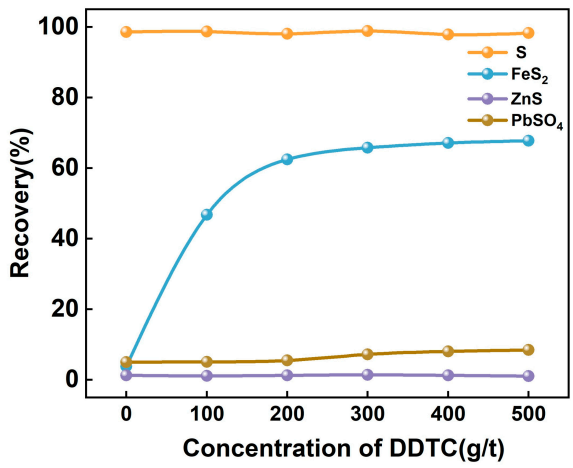

Figure 8. Pure mineral flotation. Condition: 25 °C; pH = 8; 10% pulp solution; 300 L/h airflow.

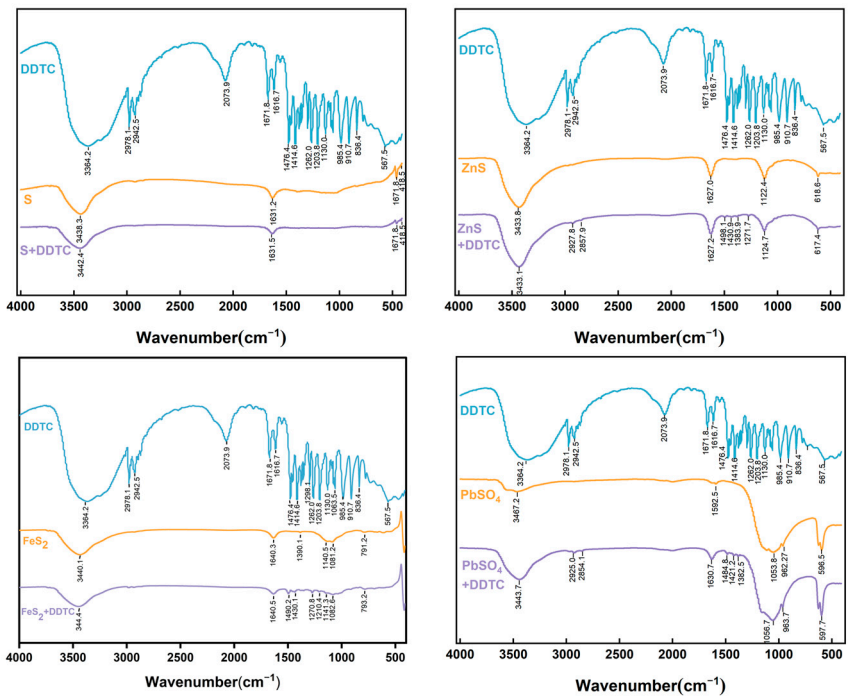

Figure 9. FT-IR spectra of DDTC adsorption on the main minerals.

3.3. Practical Bench-Scale Operation of High-Sulfur Residue Flotation

The flotation on high-sulfur residue was explored using different concentrations of DDTC to examine its practical operation. The distribution of sulfur, iron, zinc, and lead in the concentrate and tailings after flotation is shown in Figure 10. The element sulfur was mainly distributed in the concentrate, while iron, zinc, and lead were mainly distributed in the tailings (Figure 10a). With increasing DDTC concentration from 100 to 500 g/t, the contents of sulfur, iron, and zinc in the concentrate increased slightly, but lead content almost remained unchanged. This result was different from that obtained from pure mineral flotation. To explain the difference, the mineral fugacity pattern in the high-sulfur residue flotation was further analyzed. Figure 10b shows the mineral fugacity pattern in the flotation concentrate, which indicated that the concentrate was mainly composed of sulfur and sulfide. Sulfur, sphalerite, and pyrite were embedded with each other and were

difficult to separate. Figure 10c shows the mineral fugacity pattern in the flotation tailings. The tailings were composed of silica, silicate, oxide, and some sulfide. Some iron oxides were closely embedded with quartz. The elemental assignment results could be explained based on the results of the coadsorption model and SEM images of the concentrate and tailing phase. Adsorption of DDTC increased the hydrophobicity of pyrite and facilitated its floatation. Part of the sulfur and sphalerite, which embedded and wrapped the pyrite, were also floated together. This increased the contents of sulfur and zinc in the concentrate. Overall, our model predictions and practical mineral phase analysis synergistically revealed the element assignment and the flotation performance.

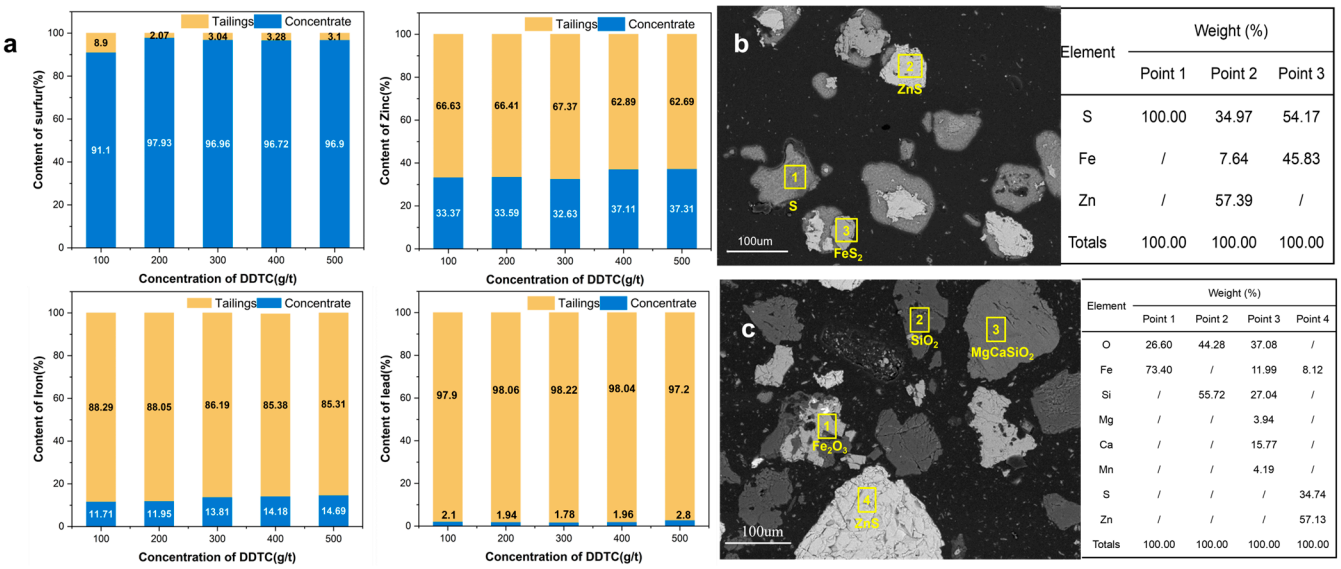

Element	Weight (%)		
	Point 1	Point 2	Point 3
S	100.00	34.97	54.17
Fe	/	7.64	45.83
Zn	/	57.39	/
Totals	100.00	100.00	100.00

Element	Weight (%)			
	Point 1	Point 2	Point 3	Point 4
O	26.60	44.28	37.08	/
Fe	73.40	/	11.99	8.12
Si	/	55.72	27.04	/
Mg	/	/	3.94	/
Ca	/	/	15.77	/
Mn	/	/	4.19	/
S	/	/	/	34.74
Zn	/	/	/	57.13
Totals	100.00	100.00	100.00	100.00

Figure 10. Element distribution behavior at different DDTC concentrations. (**a**) Element distribution; (**b**) mineral deposit pattern in the concentrate; (**c**) mineral fugacity pattern in the tailings.

4. Conclusions

This work successfully revealed the interfacial adsorption mechanism of DDTC on the four mineral phases in high-sulfur residue flotation using DFT calculation, interfacial characterization, and on-line test. The adsorption behavior results of DDTC and H_2O obtained by DFT calculation helped us construct the coadsorption model of H_2O and DDTC on sulfur, pyrite, sphalerite, and lead sulfate. On sulfur, both H_2O and DDTC had weak adsorption ability, indicating that sulfur was hydrophobic and could not be well trapped by DDTC. On sphalerite and lead sulfate surfaces, H_2O preferentially adsorbed on metal atoms than DDTC. However, on pyrite, DDTC preferentially adsorbed on metal ions than H_2O.

The pure mineral flotation operation and FT-IR results validated the coadsorption model. The pure mineral flotation result indicated the order of DDTC collection ability as follows: pyrite > lead sulfate > sphalerite > sulfur. After the addition of DDTC, the recovery of pyrite increased significantly, while the recovery of sulfur, sphalerite, and lead sulfate saw little change. The FT-IR results demonstrated that DDTC was chemisorbed on pyrite and physically adsorbed on sulfur, lead sulfate, and sphalerite. Practical bench-scale operation results indicated that the contents of pyrite, sulfur, and sphalerite in the concentrate synergistically increased with increasing DDTC concentration. This was different from the results obtained from the pure mineral flotation. This difference could be explained based on the results of the coadsorption model and SEM images of the concentrate and tailing phase. The addition of DDTC increased the hydrophobicity and floatability of pyrite. Parts of the sulfur and sphalerite, which embedded and wrapped the pyrite, were also floated together. Our model predictions and practical mineral phase analysis synergistically revealed the element assignment and flotation performance in the practical

operation. To the authors' knowledge, this is the first time such a coadsorption model has been established, which can provide theoretical foundation for the practical operation of high-sulfur residue flotation.

Supplementary Materials: The following supporting information can be downloaded at: https://www.mdpi.com/article/10.3390/pr11051568/s1, Figure S1: Electrostatic potential distribution of DDTC; Figure S2: (a) HOMO orbitals of DDTC; (b) LOMO orbitals of DDTC. Table S1: INCAR file for VASP optimization process.

Author Contributions: H.L.: Data curation, Formal analysis, Methodology, Investigation, Writing-Original Draft; J.H.: Resources, Funding acquisition; T.L.: Investigation, Validation; J.D.: Investigation, Validation; S.C.: Investigation, Validation; S.Y.: Funding acquisition, Resources; C.T.: Funding acquisition, Resources; C.W.: Project administration, Visualization, Writing—review & editing; Y.C.: Conceptualization, Funding acquisition, Supervision, Resources, Writing—review & editing. All authors have read and agreed to the published version of the manuscript.

Funding: This work was funded by the National Key Research and Development Program of China (No. 2018YFC1902005) and the Science and Technology Innovation Program of Hunan Province (No. 2021RC2002).

Data Availability Statement: Not applicable.

Acknowledgments: This work was carried out in part using hardware and software provided by the High-Performance Computing Centers of Central South University.

Conflicts of Interest: The authors declare no conflict of interest.

References

1. Liu, G.Q.; Zhang, B.S.; Dong, Z.L.; Zhang, F.; Wan, F.; Jiang, T.; Xu, B. Flotation Performance, Structure-Activity Relationship and Adsorption Mechanism of O-Isopropyl-N-Ethyl Thionocarbamate Collector for Elemental Sulfur in a High-Sulfur Residue. *Metals* **2021**, *11*, 727. [CrossRef]
2. Fan, Y.; Liu, Y.; Niu, L.; Jing, T.; Zhang, T.-a. Separation and purification of elemental sulfur from sphalerite concentrate direct leaching residue by liquid paraffin. *Hydrometallurgy* **2019**, *186*, 162–169. [CrossRef]
3. Zhou, H.; Liu, G.; Zhang, L.; Zhou, C. Mineralogical and morphological factors affecting the separation of copper and arsenic in flash copper smelting slag flotation beneficiation process. *J. Hazard. Mater.* **2021**, *401*, 123293. [CrossRef]
4. Jorjani, E.; Ghahreman, A. Challenges with elemental sulfur removal during the leaching of copper and zinc sulfides, and from the residues; a review. *Hydrometallurgy* **2017**, *171*, 333–343. [CrossRef]
5. Halfyard, J.E.; Hawboldt, K. Separation of elemental sulfur from hydrometallurgical residue: A review. *Hydrometallurgy* **2011**, *109*, 80–89. [CrossRef]
6. Wang, Z.-y.; Cai, X.-l.; Zhang, Z.-b.; Zhang, L.-b.; Wang, S.-x.; Peng, J.-h. Separation and enrichment of elemental sulfur and mercury from hydrometallurgical zinc residue using sodium sulfide. *Trans. Nonferrous Met. Soc. China* **2015**, *25*, 640–646. [CrossRef]
7. Li, H.; Wu, X.; Wang, M.; Wang, J.; Wu, S.; Yao, X.; Li, L. Separation of elemental sulfur from zinc concentrate direct leaching residue by vacuum distillation. *Sep. Purif. Technol.* **2014**, *138*, 41–46. [CrossRef]
8. Liu, G.; Yang, X.; Zhong, H. Molecular design of flotation collectors: A recent progress. *Adv. Colloid Interface Sci.* **2017**, *246*, 181–195. [CrossRef]
9. Silva, L.A.; Garrot, T.G.; Pereira, A.M.; Correia, J.C.G. Historical perspective and bibliometric analysis of molecular modeling applied in mineral flotation systems. *Miner. Eng.* **2021**, *170*, 107062. [CrossRef]
10. Ngobeni, W.A.; Hangone, G. The effect of using sodium di-methyl-dithiocarbamate as a co-collector with xanthates in the froth flotation of pentlandite containing ore from Nkomati mine in South Africa. *Miner. Eng.* **2013**, *54*, 94–99. [CrossRef]
11. Hu, Y.; Wu, M.; Liu, R.; Sun, W. A review on the electrochemistry of galena flotation. *Miner. Eng.* **2020**, *150*, 106272. [CrossRef]
12. Niu, X.; Ruan, R.; Xia, L.; Li, L.; Sun, H.; Jia, Y.; Tan, Q. Correlation of Surface Adsorption and Oxidation with a Floatability Difference of Galena and Pyrite in High-Alkaline Lime Systems. *Langmuir* **2018**, *34*, 2716–2724. [CrossRef] [PubMed]
13. Zhang, Q.; Hu, Y.H.; Xu, J.; Chen, T.J. FTIR spectroscopic study of electrochemical flotation of jamesonite-diethyldithiocarbamate system. *Trans. Nonferrous Met. Soc. China* **2006**, *16*, 493–496. [CrossRef]
14. Cui, W.Y.; Zhang, J.J.; Liu, Z.R.; Chen, J.H. Selective enhancement of jamesonite flotation using Aerophine 3418A/DDTC mixture. *Miner. Eng.* **2023**, *191*, 107934. [CrossRef]
15. Qiu, H.X.; Wu, B.Z.; Deng, J.S.; Sun, X.H.; Hu, M.Z.; Cai, J.Z.; Zheng, C. The effect of collectors on froth stability of frother: Atomic-scale study by experiments and molecular dynamics simulations. *J. Mol. Liq.* **2022**, *364*, 120035. [CrossRef]
16. Zhang, L.M.; Gao, J.D.; Khoso, S.A.; Wang, L.; Liu, Y.L.; Ge, P.; Tian, M.J.; Sun, W. A reagent scheme for galena/sphalerite flotation separation: Insights from first-principles calculations. *Miner. Eng.* **2021**, *167*, 106885. [CrossRef]

17. Chen, J.H.; Lan, L.H.; Chen, Y. Computational simulation of adsorption and thermodynamic study of xanthate, dithiophosphate and dithiocarbamate on galena and pyrite surfaces. *Miner. Eng.* **2013**, *46–47*, 136–143. [CrossRef]
18. Dai, P.L.; Wei, Z.C.; Chen, L.Z.; Liu, Y. Adsorption of butyl xanthate on arsenopyrite (001) and Cu^{2+}-activated arsenopyrite (001) surfaces: A DFT study. *Chem. Phys.* **2022**, *562*, 111668. [CrossRef]
19. Huang, X.P.; Jia, Y.; Wang, S.; Ma, X.; Cao, Z.F.; Zhong, H. Novel Sodium O-Benzythioethyl Xanthate Surfactant: Synthesis, DFT Calculation and Adsorption Mechanism on Chalcopyrite Surface. *Langmuir* **2019**, *35*, 15106–15113. [CrossRef] [PubMed]
20. Kohn, J.; Spicher, S.; Bursch, M.; Grimme, S. Quickstart guide to model structures and interactions of artificial molecular muscles with efficient computational methods. *Chem. Commun.* **2021**, *58*, 258–261. [CrossRef]
21. Pracht, P.; Bohle, F.; Grimme, S. Automated exploration of the low-energy chemical space with fast quantum chemical methods. *Phys. Chem. Chem. Phys.* **2020**, *22*, 7169–7192. [CrossRef]
22. Lu, T.; Chen, F.W. Multiwfn: A multifunctional wavefunction analyzer. *J. Comput. Chem.* **2012**, *33*, 580–592. [CrossRef]
23. Mkhonto, P.P.; Zhang, X.R.; Lu, L.; Xiong, W.; Zhu, Y.G.; Han, L.; Ngoepe, P.E. Adsorption mechanisms and effects of thiocarbamate collectors in the separation of chalcopyrite from pyrite minerals: DFT and experimental studies. *Miner. Eng.* **2022**, *176*, 107318. [CrossRef]
24. Sahraei, A.A.; Larachi, F. How Do Surface Defects Change Local Wettability of the Hydrophilic ZnS Surface? Insights into Sphalerite Flotation from Density Functional Theory Calculations. *J. Phys. Chem. C* **2021**, *125*, 998–1009. [CrossRef]
25. Lu, T.; Chen, F.W. Meaning and Functional Form of the Electron Localization Function. *Acta Phys.-Chim. Sin.* **2011**, *27*, 2786–2792.
26. Momma, K.; Izumi, F. VESTA 3 for three-dimensional visualization of crystal, volumetric and morphology data. *J. Appl. Crystallogr.* **2011**, *44*, 1272–1276. [CrossRef]
27. Vakylabad, A.B. Treatment of highly concentrated formaldehyde effluent using adsorption and ultrasonic dissociation on mesoporous copper iodide (CuI) nano-powder. *J. Environ. Manag.* **2021**, *285*, 112085. [CrossRef]
28. Sit, P.H.L.; Cohen, M.H.; Selloni, A. Interaction of Oxygen and Water with the (100) Surface of Pyrite: Mechanism of Sulfur Oxidation. *J. Phys. Chem. Lett.* **2012**, *3*, 2409–2414. [CrossRef]
29. Pollet, R.; Boehme, C.; Marx, D. Ab initio simulations of desorption and reactivity of glycine at a water-pyrite interface at "iron-sulfur world" prebiotic conditions. *Orig. Life Evol. Biosph.* **2006**, *36*, 363–379. [CrossRef]

Disclaimer/Publisher's Note: The statements, opinions and data contained in all publications are solely those of the individual author(s) and contributor(s) and not of MDPI and/or the editor(s). MDPI and/or the editor(s) disclaim responsibility for any injury to people or property resulting from any ideas, methods, instructions or products referred to in the content.